Parametric Investigation of Flow over a Rotor-Blown Wing using High-fidelity Simulations

Ullhas Udaya Hebbar
udayau@rpi.edu
Graduate Research Assistant
MOVE, RPI
Troy, NY, United States

Farhan Gandhi
gandhf@rpi.edu
Professor
MOVE, RPI
Troy, NY, United States

Onkar Sahni
sahni@rpi.edu
Associate Professor
MOVE, RPI
Troy, NY, United States

ABSTRACT

This study models an infinite rotor-wing unit based on the CRC-20 quad-rotor bi-plane at an angle of attack of 8° and rotor modeled using the actuator line method (ALM). Parametric variations to the rotor-wing geometry are considered. These include rotor-wing chordwise separation, rotor-wing vertical offset and rotor-rotor spanwise separation. Large eddy simulation (LES) and delayed detached eddy simulation (DDES) approaches with and without the transition model are used to analyze the baseline configuration. DDES with the transition model is found to compare well with LES and is selected for the parametric study to balance the computational cost. Compared to isolated wing and rotor cases, baseline rotor-wing case shows 5.46% lower power loading, 14.42% higher lift and 4.45% higher L/D ratio. From the parametric study, varying the rotor-wing chordwise spacing did not significantly influence rotor power loading but placing rotor further from the wing improved L/D ratio by 7.64% compared to baseline due to reduction in sectional drag. The rotor-wing vertical offset cases show that placing the rotor below the wing significantly reduces the L/D ratio while placing it above yields similar L/D ratio to baseline but lowers the power loading by 6.69%. Finally, the spanwise rotor-rotor separation cases show that higher separation yields a 5.66% improvement to L/D ratio with no effect on the rotor power loading, again due to reduction in sectional drag.

INTRODUCTION

The burgeoning field of vertical take-off and landing (VTOL) has seen several recent advances and accomplishments. Aided by simultaneous developments in electric storage and propulsion technologies, recent years have seen an advent of electric VTOL (eVTOL) aircraft. However, the significantly lower energy densities shown by batteries compared to their convential hydrocarbon counterparts necessitates optimum aerodynamic performance from these aircraft. In order to accelerate developments in the unmanned aerial systems (UAS) field and foster collaboration between researchers in the area, the US army has recently introduced common research configurations (CRC) [1]. The 20 lb. gross weight CRC-20 is a quad-rotor bi-plane concept developed under this platform and forms the focus of this work.

Lifting surfaces and multiple propellers operating in close proximity generally leads to complex aerodynamic interactions, a feature certainly observed in the rotor-blown wing CRC-20 concept. A wide range of assumptions and model selections are made for the physics of such problems by the rotorcraft computational fluid dynamics community. These include different Navier-Stokes formulations, various approaches to the modeling of propellers as well as different choices to the turbulence modeling employed for the simulations. A common approach fully resolves the propeller blade geometry and handles blade rotation with either an overset mesh approach or a sliding mesh interface. Another approach which lowers simulation cost is the use of an actuator disk/line model (ADM/ALM) for the propellers where fictitious loads - or more specifically - momentum sources are applied in a steady (ADM) or unsteady (ALM) fashion. Aref *et al.* [2] used the DDES turbulence model along with a blade resolved rotor with an overset grid to study both single and dual propeller-blown wing configurations. Local increases in lift on the wing were observed in this study as well as delay in flow separation and local stall over the wing downstream of the propellers. Fischer *et al.* [3] analyzed the interaction of a wing with multiple (up to 16) propellers. Different configurations were considered by the authors, including over-the-wing and leading edge mounted propellers. The unsteady Reynolds averaged Navier-Stokes (URANS) turbulence model was employed along with ALM for the rotor blades. Lift increases to the tune of 50% were observed, especially in the over-the-wing configuration with adjacent counter-

Presented at the Vertical Flight Society's 78th Annual Forum & Technology Display, Ft. Worth, Texas, USA, May 10–12, 2022.

rotating propellers where the highest gains were measured. Similarly, Misiorowski *et al.* [4] studied the same CRC-20 concept with a blade resolved propeller modeled using an overset grid and a DDES model for the turbulence closure. Again, lift increases of $\sim 20\%$ were observed compared to the isolated wing with minor effects of the wing on rotor performance. This study also observed dramatic increases in lift on varying rotor RPM, for example, operating the rotor at 2x RPM yielded 100% increases in the measured lift compared to the baseline case. The authors of the current work previously analyzed the infinite rotor-wing based on the CRC-20 with different turbulence models including LES, DDES and URANS with an ALM-based rotor model for a higher angle of attack of 12° [5]. Cycle-averaged rotor quantities were found to be similar between the turbulence models while wing drag was found to be over-predicted by the DDES and URANS based cases. Additionally, several papers [6, 7, 8] have analyzed wingtip-mounted propellers where despite the lower lift generation compared to their inboard counterparts, these configurations yield a significantly smaller drag penalty, i.e, when the propeller counteracts the wingtip vortex.

In the present study, the ALM approach [9, 10] was employed for the rotor blades owing to its attractive computational cost, ease of numerical implementation, as well as its ability to accurately resolve relevant flow features including the unsteadiness and key flow structures in the rotor wake. The latter is necessary for accurate prediction of the wing aerodynamic performance with an upstream rotor. Note that an even more attractive alternate from a computational viewpoint is the ADM approach [11], however it cannot capture the unsteadiness and relevant flow structures in the rotor wake. In this study, the wing is represented using a body-fitted unstructured mesh. The goal of this work is to comprehensively analyze an infinite-wing configuration of the CRC-20 using different turbulence modeling approaches including the large-eddy simulation (LES) as well as the delayed detached eddy simulation (DDES). Delayed detached eddy simulations are performed with and without the transition model. These three choices (including two for DDES with and without the transition model and one for LES) are considered for the baseline configuration since they are computationally tractable and yet provide high fidelity. LES is computationally expensive, however, it can accurately capture relevant flow features over the wing, specifically transition to turbulence of the boundary layer flow [12, 13]. DDES with the transition model is found to compare better with the LES. Thus, in order to balance the computational cost, DDES with the transition model is used to perform the parametric study with variations in the geometry. This is particularly crucial due to the expected spanwise non-uniformity in transition over the wing blown by the upstream rotor.

METHODOLOGY

Numerical formulation

Incompressible Navier-Stokes equations are used in this work. The strong form of the equations is given as

$$\begin{aligned} &u_{k,k} = 0 \\ &u_{i,t} + (u_j - u_j^m)u_{i,j} = -p_{,i} + \tau^v_{ij,j} + f_i \end{aligned} \tag{1}$$

where u_i is the velocity vector, u_i^m is the mesh velocity vector (which is used in a moving mesh case), p is the pressure (scaled by the constant density), $\tau^v_{ij} = 2\nu S_{ij}$ is the symmetric (Newtonian) viscous stress tensor (scaled by the density), ν is the kinematic viscosity, $S_{ij} = 0.5(u_{i,j} + u_{j,i})$ is the strain-rate tensor, and f_i is the body force vector (per unit mass). Note that Einstein summation notation is used.

The weak form is stated as follows: find $\mathbf{u} \in \mathscr{S}$ and $p \in \mathscr{P}$ such that

$$\begin{aligned} B(\{w_i,q\},\{u_i,p\};u_l^m) = &\int_\Omega [w_i(u_{i,t} + u_i u^m_{j,j}) \\ &+ w_{i,j}(-u_i(u_j - u_j^m) + \tau^v_{ij} - p\delta_{ij}) - q_{,k}u_k]\, d\Omega \\ &+ \int_{\Gamma_h} [w_i(u_i(u_j - u_j^m) - \tau^v_{ij} + p\delta_{ij})n_j + q u_k n_k]\, d\Gamma_h \\ &= \int_\Omega w_i f_i d\Omega \end{aligned} \tag{2}$$

for all $\mathbf{w} \in \mathscr{W}$ and $q \in \mathscr{P}$. $\mathscr{S}$ and $\mathscr{P}$ are suitable trial/solution spaces and $\mathscr{W}$ is the test/weight space. $\mathbf{w}$ and q are the weight functions for the velocity and pressure variables, respectively. Ω is the spatial domain and Γ_h is the portion of the domain the boundary with Neumann or natural boundary conditions.

The above weak form can be written concisely as find $\boldsymbol{U} \in \mathscr{U}$ such that

$$B(\boldsymbol{W},\boldsymbol{U};u_l^m) = (\boldsymbol{W},\boldsymbol{F}) \tag{3}$$

for all $\boldsymbol{W} = [\mathbf{w},q]^T \in \mathscr{V}$. $\boldsymbol{U} = [\mathbf{u},p]^T$ is the vector of unknown solution variables and $\boldsymbol{F} = [\mathbf{f},0]^T$ is the source vector. The solution and weight spaces are: $\mathscr{U} = \{\boldsymbol{U} = [\mathbf{u},q]^T | \mathbf{u} \in \mathscr{S}; p \in \mathscr{P}\}$ and $\mathscr{V} = \{\boldsymbol{W} = [\mathbf{w},q]^T | \mathbf{w} \in \mathscr{W}; q \in \mathscr{P}\}$, respectively.

Throughout this text $B(\cdot,\cdot)$ is used to represent the semi-linear form that is linear in its first argument and $(\cdot,\cdot)$ is

used to denote the L_2 inner product. $B(\boldsymbol{W},\boldsymbol{U};u_l^m)$ is split into bilinear and semi-linear terms as shown below.

$$B(\boldsymbol{W},\boldsymbol{U};u_l^m) = B_1(\boldsymbol{W},\boldsymbol{U};u_l^m) + B_2(\boldsymbol{W},\boldsymbol{U}) = (\boldsymbol{W},\boldsymbol{F}) \quad (4)$$

where $B_1(\boldsymbol{W},\boldsymbol{U};u_l^m)$ contains the bilinear terms and $B_2(\boldsymbol{W},\boldsymbol{U})$ consists of the semi-linear terms. These are defined as

$$\begin{aligned} B_1(\boldsymbol{W},\boldsymbol{U};u_l^m) = & \\ & \int_\Omega [w_i(u_{i,t} + u_i u_{j,j}^m) + w_{i,j}(u_i u_j^m + \tau_{ij}^v - p\delta_{ij}) - q_{,k}u_k]\, d\Omega \\ & + \int_{\Gamma_h} [w_i(-u_i u_j^m - \tau_{ij}^v + p\delta_{ij})n_j + q u_k n_k]\, d\Gamma_h \end{aligned} \quad (5)$$

$$B_2(\boldsymbol{W},\boldsymbol{U}) = -\int_\Omega w_{i,j} u_i u_j d\Omega + \int_{\Gamma_h} w_i u_i u_j n_j d\Gamma_h \quad (6)$$

The Galerkin weak form is obtained by considering the finite-dimensional or discrete solution spaces $\mathscr{S}^h \subset \mathscr{S}$ and $\mathscr{P}^h \subset \mathscr{P}$ and the weight space $\mathscr{W}^h \subset \mathscr{W}$, where the superscript h is used as a mesh parameter to denote discretized spaces and variables in a finite element context. Using these spaces, $\mathscr{U}^h = \{\boldsymbol{U}^h = [\mathbf{u}^h, p^h]^T | \mathbf{u}^h \in \mathscr{S}^h; p^h \in \mathscr{P}^h\}$ and $\mathscr{V}^h = \{\boldsymbol{W}^h = [\mathbf{w}^h, q^h]^T | \mathbf{w}^h \in \mathscr{W}^h; q^h \in \mathscr{P}^h\}$ are defined. The Galerkin weak form is then stated concisely as: find $\boldsymbol{U}^h \in \mathscr{U}^h$ such that

$$B(\boldsymbol{W}^h,\boldsymbol{U}^h) = (\boldsymbol{W}^h,\boldsymbol{F}) \quad (7)$$

for all $\boldsymbol{W}^h \in \mathscr{V}^h$. Note for brevity we have dropped u_l^m term in the arguments of the semi-linear form. The Galerkin weak formulation corresponds to a method for direct numerical simulation since no modeling is employed. However, when the finite-dimensional spaces are incapable of representing the fine/small scales, the Galerkin formulation yields an inaccurate solution. A model term is added to overcome this difficulty, e.g., as done in the residual-based variational multiscale (RBVMS) formulation.

In RBVMS, a set of model terms is added to the Galerkin weak form that results in the following variational formulation: find $\boldsymbol{U}^h \in \mathscr{U}^h$ such that

$$B(\boldsymbol{W}^h,\boldsymbol{U}^h) + M_{rbvms}(\boldsymbol{W}^h,\boldsymbol{U}^h) = (\boldsymbol{W}^h,\boldsymbol{F}) \quad (8)$$

for all $\boldsymbol{W}^h \in \mathscr{V}^h$. M_{rbvms} represents the set of model terms due to the RBVMS approach.

A scale separation is used to decompose the solution and weight spaces as $\mathscr{S} = \mathscr{S}^h \oplus \mathscr{S}'$ and $\mathscr{P} = \mathscr{P}^h \oplus \mathscr{P}'$, and $\mathscr{W} = \mathscr{W}^h \oplus \mathscr{W}'$, respectively. Thus, the solution and weight functions are decomposed as $u_i = u_i^h + u_i'$ and $p = p^h + p'$ or $\boldsymbol{U} = \boldsymbol{U}^h + \boldsymbol{U}'$, and $w_i = w_i^h + w_i'$ and $q = q^h + q'$ or $\boldsymbol{W} = \boldsymbol{W}^h + \boldsymbol{W}'$, respectively. Note that coarse-scale or resolved quantities are denoted by $(\cdot)^h$ and fine-scale or unresolved quantities by $(\cdot)'$. The coarse-scale quantities are resolved by the grid whereas the effects of the fine scales on the coarse scales are modeled. In RBVMS, the fine scales are modeled as a function of the strong-form residual due to the coarse-scale solution. This is represented abstractly as $\boldsymbol{U}' = \mathscr{F}(\boldsymbol{R}(\boldsymbol{U}^h);\boldsymbol{U}^h)$, where $\boldsymbol{R}(\cdot) = [\boldsymbol{R}^m(\cdot), R^c(\cdot)]^T$ is the strong-form residual of the equations with $\boldsymbol{R}^m(\cdot)$ (or $R_i^m(\cdot)$) and $R^c(\cdot)$ as those of the momentum and continuity equations, respectively. Specifically, the fine-scale quantities are modeled as $u_i' \approx -\tau_M R_i^m(u_k^h, p^h; u_l^m)$ and $p' \approx -\tau_C R^c(u_k^h)$, where τ_C and τ_M are stabilization parameters (e.g., see details in Tran and Sahni [14]). This provides a closure to the coarse-scale problem as it involves coarse-scale solution as the only unknown. This is why $M_{rbvms}(\boldsymbol{W}^h,\boldsymbol{U}^h)$ is written only in terms of the unknown coarse-scale solution $\boldsymbol{U}^h$. Note that RBVMS formulation provides the basis for the stabilized finite element methods.

RBVMS formulation is used for all simulations with different turbulence modeling approaches. For the baseline configuration, three modeling approaches are used: DDES with and without transition model, and LES. DDES with the transition model is found to compare better with the LES. This is expected due to the spanwise non-uniformity in transition over the wing blown by the upstream rotor. Thus, in order to balance the computational cost, DDES with the transition model is used to perform the parametric study with variations in the geometry.

DDES approach is based on the Spalart-Allmaras (SA) turbulence model near the wing while it uses a static LES-type subgrid-scale model away from the wing (e.g., in the wake). For transition modeling, γ model is used. DDES cases are conducted using the commercial Navier-Stokes solver: AcuSolve®, which has been extensively validated for external aerodynamic flows [4, 15, 16] and even for transitional flows [17, 18]. LES is based on an in-house flow solver [12, 13, 14]. It employs the RBVMS approach for LES along with an appropriate mesh resolution including the wall-resolved treatment on the wing.

Numerical discretization and problem setup

The complete CRC-20 case is a quad-rotor biplane system. For this work, a half-wing unit of the CRC-20 concept with one rotor (as shown in Fig. 1) is simulated as an infinite co-rotating rotor-blown wing by making use of periodic condition in the spanwise direction. For the baseline configuration, the 60.9 cm (24 in) diameter rotor is placed at the center of the half-wing unit, and 6.98

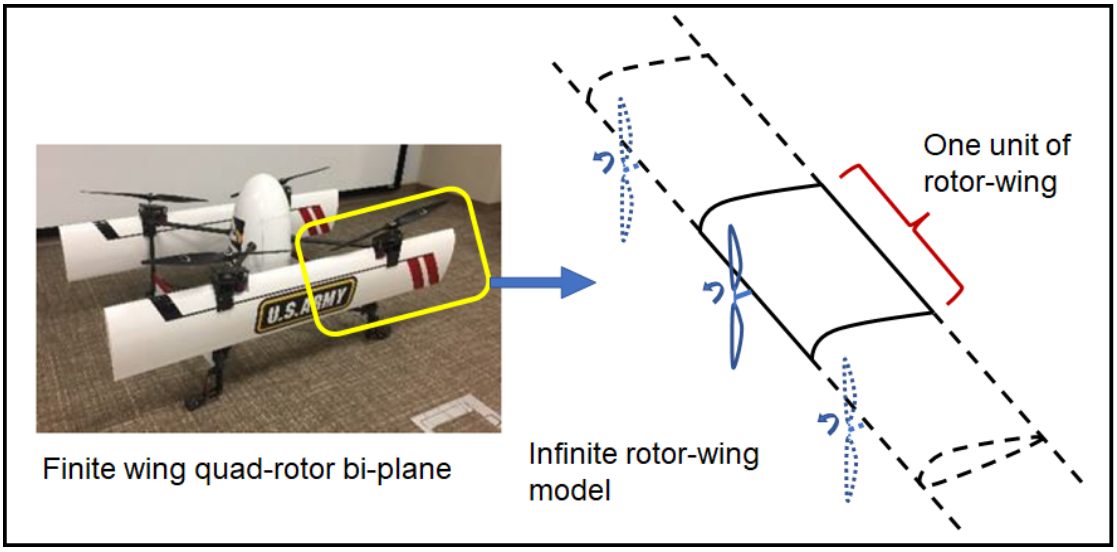

Figure 1: CRC-20 prototype on the left side (where half-unit is highlighted) and schematic of the current rotor-blown wing unit on the right

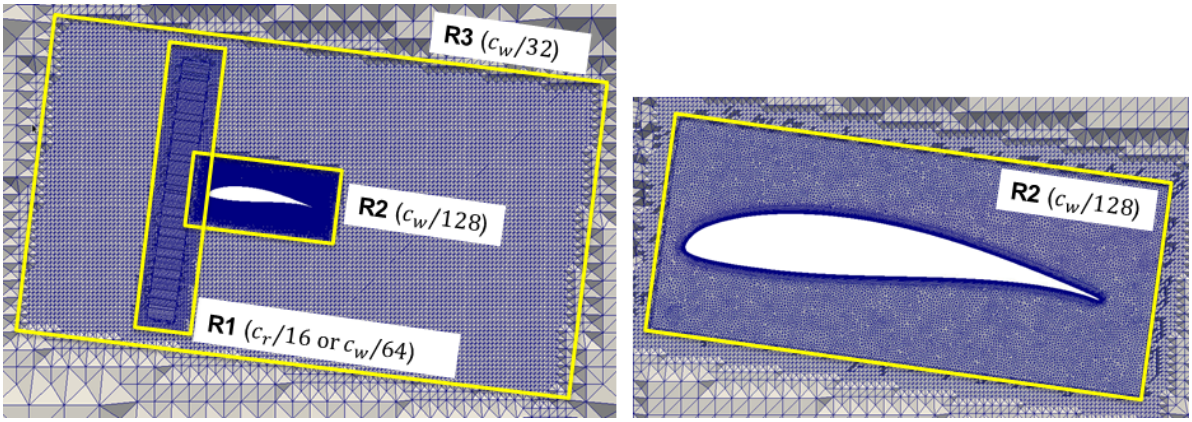

Figure 2: Mesh used for ALM-LES simulation with a zoom around the wing

cm (2.75 in) upstream of the leading edge of the half-wing with a span of 76.2 cm (30 in). The root chord of the blade is $c_r = 6.15$ cm. The wing itself is composed of an untapered and untwisted airfoil cross-section corresponding to the Wortmann FX 63-137 airfoil with a chord of $c_w = 25.14$ cm (9.9 in). It should be noted that the rotor axis is aligned with the chord line of the wing, and the rotor is based on a scaled up version of the straight-up imaging (SUI) endurance rotor [19]. A cruise condition is simulated for an 8° angle-of-attack (AOA), a freestream velocity of 12.34 m/s (24 kts) and a counter-clockwise rotational speed of 2900 RPM for the propeller.

In the parametric study, first the chordwise distance from the rotor center to the leading edge (LE) of the wing is considered. This is expected to significantly change the effect of the wing on the rotor:

- Baseline: 6.98 cm
- Reduced spacing (nearLE): 5.0275 cm
- Increased spacing (farLE): 8.9375 cm

Next, the rotor vertical offset (perpendicular to wing chordline/planform) is considered. This variation is expected to significantly alter both wing and rotor quantities:

- Baseline: 0 cm
- Rotor offset +Y (rotorUp): +7.6125 cm
- Rotor offset -Y (rotorDown): -7.6125 cm

Finally, tip-to-tip spacing of adjacent rotors is varied. Due to the periodic conditions in the spanwise direction, this is equivalent to increasing/decreasing the span of the wing used in the simulation. This is expected to influence spanwise variation in lift and drag of the wing:

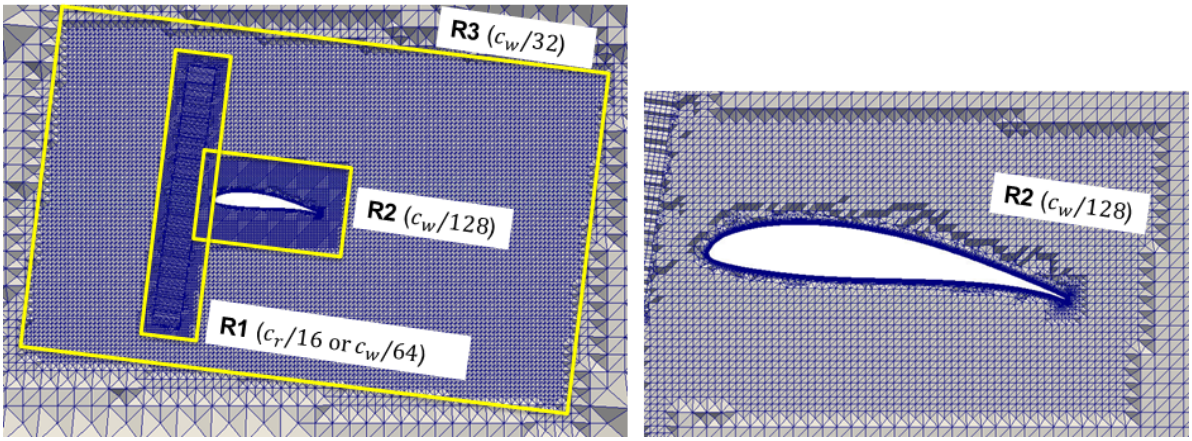

Figure 3: Mesh used for ALM-DES simulation with a zoom around the wing

- Baseline tip-to-tip: 15.3 cm
- Reduced tip-to-tip: 7.65 cm
- Increased tip-to-tip: 22.95 cm

The mesh used for the ALM-LES simulation in this paper is shown in Fig. 2. A boundary layer mesh is generated over the wing surface with 34 layers and a first layer height corresponding to $\Delta y^+ \approx 0.5$ (at the maximum). On the wing surface, the resolution of the boundary layer mesh is set to be up to $\Delta x^+ \approx 100$ and $\Delta z^+ \approx 50$, which are deemed appropriate for LES. In addition, several refinement zones are used. A refinement zone (R1) is defined around the rotor with a resolution of $c_r/16 \approx c_w/64$. Another refinement zone (R2) with a resolution of $c_w/128$ is defined around the wing. Finally, one more refinement zone (R3) surrounds the rotor and wing with a resolution of $c_w/32$ to sufficiently capture the wake of the rotor washing over the wing. The ALM-LES mesh contains about 55 million elements.

Fig. 3 shows the mesh used for the ALM-DDES simulations. Similar to the ALM-LES mesh, a boundary layer mesh is generated over the wing surface with 34 layers and a first layer height corresponding to $\Delta y^+ \approx 0.5$ (at the maximum). On the wing surface, the resolution of the boundary layer mesh is set to be up to $\Delta x^+ \sim \Delta z^+ \approx 300$, which are deemed appropriate for the DDES simulations. This resolution is lower than the LES simulation as the DDES models employ RANS-based modeling near the wing. The refinement zones R1 (around rotor) and R3 (around rotor and wing) remain the same as the LES mesh to capture the evolution of rotor-related vortical structures, while the resolution of refinement zone (R2) around the wing is set to be coarser to $c_w/64$ for the DDES cases. The ALM-DDES mesh contains roughly 23 million elements.

A timestep corresponding to 2° rotation of the propeller is used for the second-order generalized-α implicit time integration scheme [20]. Periodic condition is used in the span, while an axial velocity of 12.34 m/s is imposed at the inlet. The outlet is located 20 chord-lengths away from the wing and set to natural pressure condition. Slip condition with no penetration is imposed for the upper and lower surfaces of the domain. Finally, a no-slip condition is imposed on the airfoil surface. All runs are performed on a cluster, using 6 to 12 nodes each with 24 AMD Epyc 7451 processors (i.e., 144 to 288 cores are used), which is a part of the Center for Computational Innovations (CCI) at Rensselaer Polytechnic Institute.

Rotor model: ALM

The propeller is modeled by imposing time-varying momentum sources. Specifically, initial load distribution is computed from a lower-order model based on the Peters-He dynamic inflow as available an in-house comprehensive analysis tool: RMAC [21]. These loads are imposed on actuator lines representing the two blades in the rotor and are updated over the simulation based on the local flow around the rotor thus capturing rotor-wing interactional aerodynamics. Within the ALM framework, the loads over actuator lines are applied as volumetric source terms over a region defined around them at any given instance. The width of such a region is chosen such that $\gamma = c_r$ over the entire span of the blade. Furthermore, to avoid sharp discontinuities in the load distribution, the loads are smeared in the normal and tangential directions over a width of 2γ. In summary, the volumetric source term can be written as: $\mathbf{f_{3D}}^{CFD} = \mathbf{f_{1D}}^{BET}(r)\delta(n)\delta(\theta)$, where $f_{1D}^{BET}(r)$ is the computed 1D load distribution (initially from RMAC, and updated during the simulation), while $\delta(n)$ or $\delta(\theta)$ is a cubic spline distribution function (for $|s| \leq \gamma$) with unit area and is de-

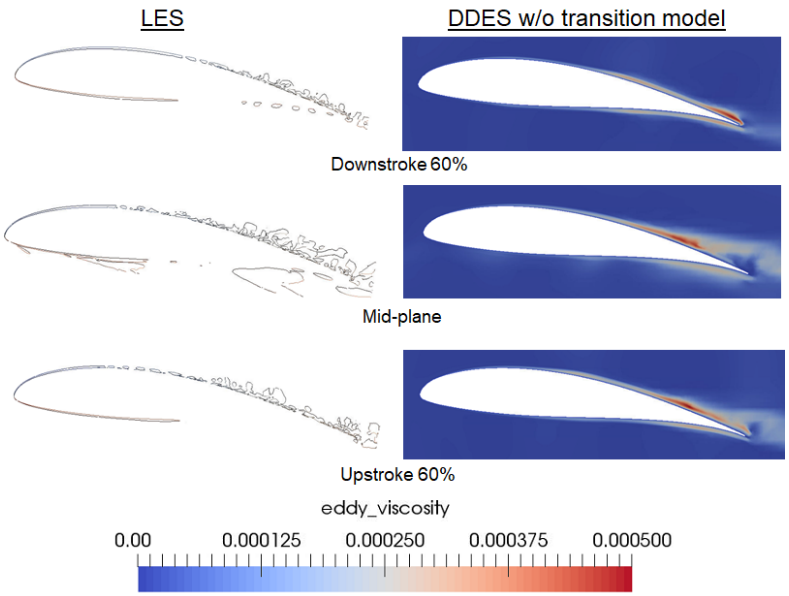

Figure 4: Comparison of wing slices: ALM-LES vs. ALM-DES without transition model

fined as: $t_0 = \frac{s+\gamma}{\gamma}$; $\delta(s) = \frac{1}{\gamma}\left[-2t_0^3 + 3t_0^2\right]$; $s < 0$ and $t_0 = \frac{s}{\gamma}$; $\delta(s) = \frac{1}{\gamma}\left[2t_0^3 - 3t_0^2 + 1\right]$; $s \geq 0$.

RESULTS AND DISCUSSION

The results from this study are organized as follows: first, results from the baseline configuration are compared between the ALM-LES case and the ALM-DDES cases with and without the transition model. DDES with the transition model is found to compare better with the LES. Thus, in order to balance the computational cost, DDES with the transition model is used subsequently. Before performing the parametric study, the baseline case is compared with the isolated wing and isolated rotor cases to establish the rotor-wing interactional aerodynamics. This is followed by the results from the geometric parameter variation starting with the rotor-wing chordwise separation, then the rotor-wing vertical offset and finally the rotor-rotor separation. For the ALM-LES case, the simulation is carried out for 30 propeller revolutions with about 25 revolutions required to attain convergence in rotor and wing quantities, and thus, data averaged over the last 5 revolutions are presented. On the other hand, the ALM-DDES cases required about 8 revolutions for convergence and subsequently two more revolutions are used to obtain averaged data.

Comparison of ALM-LES with ALM-DDES with and without transition model

In a problem involving complex interactional aerodynamics such as the rotor-blown wing and at a Reynolds number of ~ 250000 where transitional behavior is expected over the wing, it is important to accurately model the transition of the boundary layer over the wing. Figs. 4 and 5 show comparisons of ALM-LES and ALM-DDES cases without and with transition model, respectively. The left half of both figures shows slices of the Q-criterion isosurface, a qualitative indicator of vortices, from the ALM-LES. We use this qualitative indicator for the current LES (based on the RBVMS method) to detect transition of the boundary layer over the wing. It highlights that the transition occurs near the trailing edge and exhibits spanwise non-uniformity. Three different spanwise locations on the wing are considered: 60% of the half-wing section on the downstroke side of the rotor, where the rotor-induced downwash is present and transition to turbulence occurs in a delayed fashion; 60% of the half-wing section on the upstroke side of the rotor where the induced upwash increases the local angle-of-attack over the wing and an earlier transition is observed; and middle of the wing section that experiences highly turbulent vortical flow emanating from the root of the rotor and a higher turbulence is observed in the boundary layer over the wing surface at this section. The comparison to ALM-DDES without the transition model is done using the eddy-viscosity, which shows the transition to turbulence via the deeper red color. Overall the behaviour of boundary layer shows

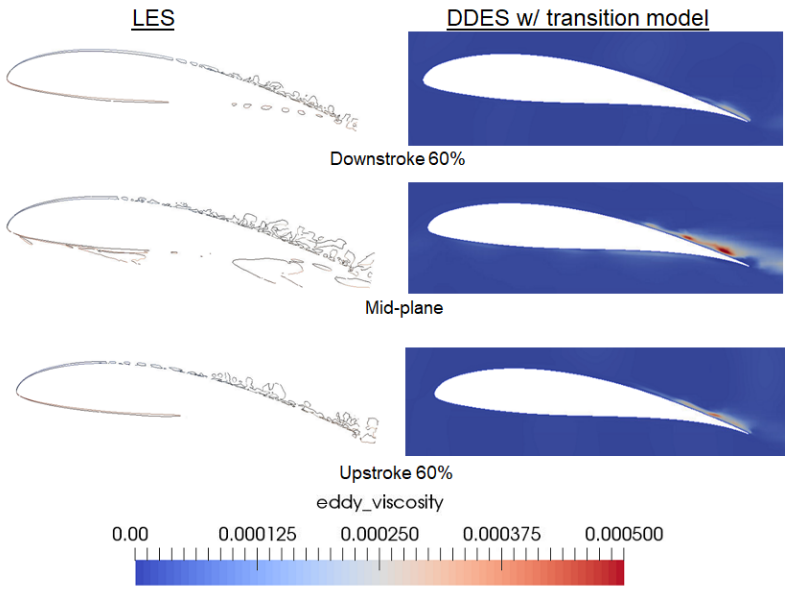

Figure 5: Comparison of wing slices: ALM-LES vs. ALM-DES with transition model

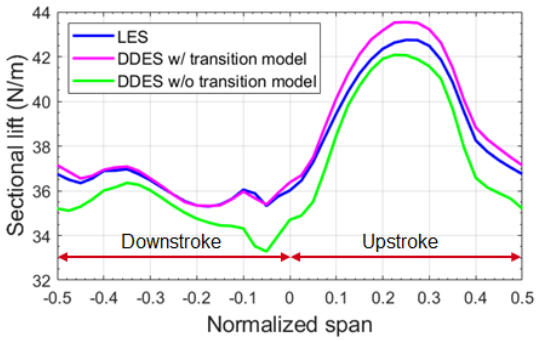

Figure 6: Comparison of spanwise lift: ALM-LES vs. ALM-DES with and without transition model

spanwise variations, however, the location when eddy-viscosity becomes reasonably high is predicted to be similar at each of these three sections. In contrast, Fig. 5 compares ALM-LES and ALM-DDES with the transition model. The eddy-viscosity contours from the three sections show overall variations as well as significant differences in the location when eddy-viscosity becomes reasonably high (in a similar fashion as the ALM-LES case).

A more quantitative comparison between ALM-LES and ALM-DDES with and without the transition model is presented using time-averaged sectional wing lift in Fig. 6. Clearly, there is a distinct spanwise variation in lift for all three cases due to the effect of the rotor wake on the wing. The upstroke side shows a peak between 0.2 and 0.3 of normalized span for all three cases, this is due to the induced upwash over the wing resulting in a local increase in angle of attack. However, ALM-DDES with the transition model shows good overall agreement with ALM-LES, which is in contrast to ALM-DDES without the transition model that underpredicts the lift over the entire wing span.

Comparison of baseline configuration with isolated wing/rotor

For a better understanding of the interactional aerodynamics between the rotor and wing in the CRC20 baseline configuration, comparisons are drawn between the rotor-blown wing simulation with the isolated rotor and isolated wing simulations.

Fig. 7 shows phase-averaged integrated rotor thrust and power. The phase averaging is done over 2 revolutions of the rotor. For a symmetric two-bladed rotor, this corresponds to 4 samples collected for each phase in a cycle, and therefore, phase-averaged data for half a cycle (i.e., up to 180° phase) is presented. Baseline configuration of the rotor-blown wing case shows significant variation over the cycle. It is referred to as base in this and subsequent figures. Both the thrust and power curves reach their peak around the 90° phase, where the blades are aligned with the wing. Comparing the cycle-averaged thrust and power, the rotor-blown wing case shows 7.6 N of thrust, which is 3.3% lower than the isolated rotor thrust of 7.859 N, while showing 231.1 W of power which is 2.45% higher compared to the isolated rotor power of 225.56 W. In terms of power loading (ratio of thrust produced to required power), rotor-blown wing case shows a

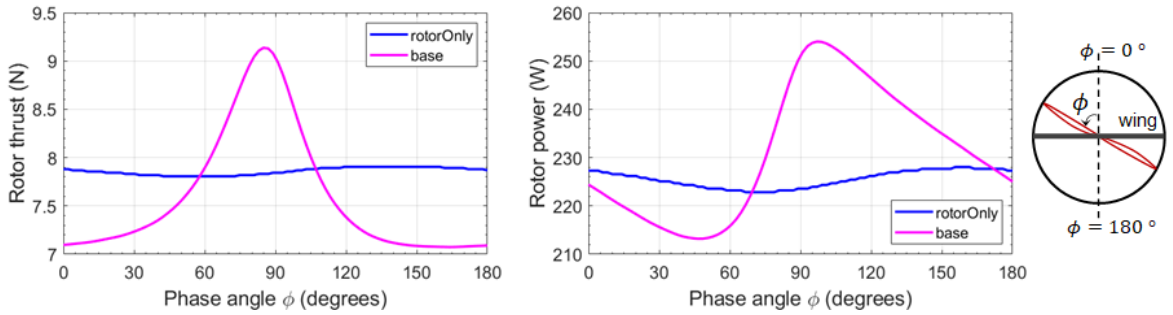

Figure 7: Comparison of phase-averaged rotor thrust and power: rotor-blown wing vs. isolated rotor

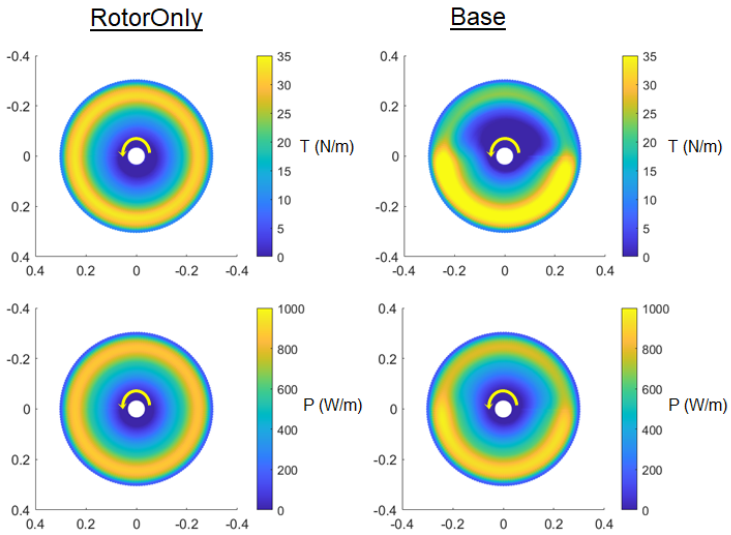

Figure 8: Comparison of thrust and power disk plots: rotor-blown wing vs. isolated rotor

power loading of 0.0329 which is 5.46% lower than the isolated rotor case of 0.0348.

Fig. 8 compares thrust and power over the rotor disk between the rotor-blown wing and isolated rotor cases. The isolated rotor thrust appears marginally higher on the downstroke side compared to the upstroke side due to the disparity created by the $V_\infty sin(\alpha)$ component of the freestream velocity (V_∞), where α is the angle of attack. This effect is also present in the isolated rotor power. In contrast, the rotor-blown wing thrust plot shows a significant disparity above and below the wing with much higher values below the wing. This effect is due to the effect of wing circulation on the rotor. The wing induces upwash on the rotor portion below the centerline thereby increasing the local angle of attack on the blades while the opposite is true above the centerline.

Fig. 9 shows the time-averaged sectional lift and drag comparison between the baseline rotor-blown wing and isolated wing cases. The sectional lift for the rotor-blown wing case on the left plane is higher than the isolated wing over the entire span. The peak lift on the downstroke side at about -0.35 of the normalized span is 10.6% higher than the isolated wing lift while the peak lift on the upstroke side at about 0.25 of the normalized span is 29.86% higher than the isolated wing lift. The overall time-averaged wing lift for the rotor-blown wing case is found to be 29.18 N which is 14.52% higher than the isolated wing case at 25.48 N. Looking at the sectional drag on the right panel, the rotor-wing case shows higher drag compared to the isolated wing over most of the downstroke side where the peak drag at roughly -0.3 of the normalized span is 127.75% higher than the isolated wing drag. However, the drag on the upstroke side is overall lower than the isolated wing except the peak drag which is nearly equal to the isolated wing drag. Looking at the time-averaged drag for the wing, the rotor-wing case results in 1.413 N which is 9.62% higher than the 1.289 N for the isolated wing. Overall, looking at the L/D ratio for the two cases, the baseline configuration of the rotor-wing case shows a value of 20.65, which is 4.45% higher

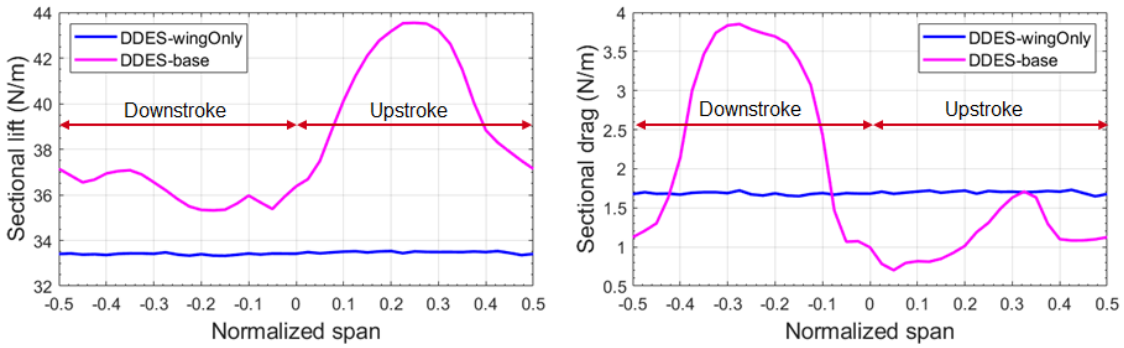

Figure 9: Comparison of spanwise lift and drag: rotor-blown wing vs. isolated wing

than the isolated wing L/D ratio of 19.77. Note that these values may vary significantly when considering a finite wing configuration instead of an idealized infinite wing considered in this study.

Variation of rotor-wing chordwise separation

In this subsection, we consider the rotor-wing or rotor-leading edge separation along the chordwise direction as described earlier. The major effect is expected to be on the rotor quantities, especially around blade-wing passage.

Fig. 10 shows a comparison of instantaneous Q-criterion isosurfaces colored by pressure for the three chordwise separation cases. Some clear differences can be observed, particularly in the root and tip vortices shed by the rotor. The LEfar case shows diminished interruption of the rotor tip vortices by the wing on both the upstroke and downstroke sides. On the other hand, the LEnear case shows increased interruption and in fact a clear disruption of the tip vortex can be observed on the upstroke side of the wing. Some differences can also be seen near the center of the wing where the root vortices appear less disrupted in the LEfar case.

For a comparison of rotor and wing quantities, Fig. 11 shows a comparison of the phase-averaged thrust and power integrated over the rotor. Distinct differences can be observed near the rotor-wing passage between $\phi = 60^\circ$ and $\phi = 120^\circ$ for the integrated thrust. The LEnear case shows the highest peak thrust, which is 8.9% higher than the baseline case while the LEfar case shows a 6.1% lower peak thrust as compared to baseline. While there are differences away from this region of interest in the plot, they are rather small. The LEnear case shows a cycle-averaged thrust of 7.68 N which is 1.02% higher than the baseline thrust of 7.6 N, while the LEfar case shows 7.62 N which is 0.27% higher than baseline. The cycle-averaged power shows a similar trend to thrust with LEnear showing 231.67 W which is 0.25% higher than the baseline power of 231.1 W while LEfar shows a cycle-averaged power which is within 0.1% of the baseline.

Fig. 12 compares thrust and power between the three cases. As expected, the LEnear case shows higher values of thrust and power near the blade-wing passage compared to baseline while the converse is true for the LEfar case. Another feature to be noted is the larger blue region in the thrust for the LEnear case above the wing which leads to the lower thrust seen away from blade-wing passage for this case. Fig. 13 shows the time-averaged sectional lift and drag comparison for the rotor-wing chordwise separation cases. The sectional lift curves shown on the left panel are quite similar for the three cases with the LEnear case showing the highest lift and the LEfar case showing the lowest. Time-averaged wing lift for the LEnear case is 29.33 N which is 0.51% higher than baseline while LEfar shows 28.96 N of wing lift which is 0.75% lower than baseline. The sectional drag curves on the right panel show a similar trend to the lift, although the LEfar case does show a significantly lower peak drag on the downstroke side, specifically by 7.79%, as compared to the baseline, while LEnear shows a 2.58% higher peak drag. For time-averaged drag over the wing, LEnear shows 1.489 N which is 5.38% higher than the baseline case of 1.413 N. On the other hand, the LEfar case shows 1.303 N of wing drag which is 7.78% lower than the baseline.

In order to summarize the differences in rotor-wing quantities between the three cases, aggregate quantities are constructed for the rotor and wing. Power loading is considered for the rotor, which indicates the thrust produced by the rotor normalized by the power required to produce that thrust. For the wing, the well-known L/D ratio is used. These quantities are summarized for the rotor-wing chordwise separation cases in Table 1. Clearly, while the power loading is very close for all three cases, the LEfar case shows 7.64% higher L/D ratio as compared to baseline while LEnear case shows 4.61% lower L/D ratio as

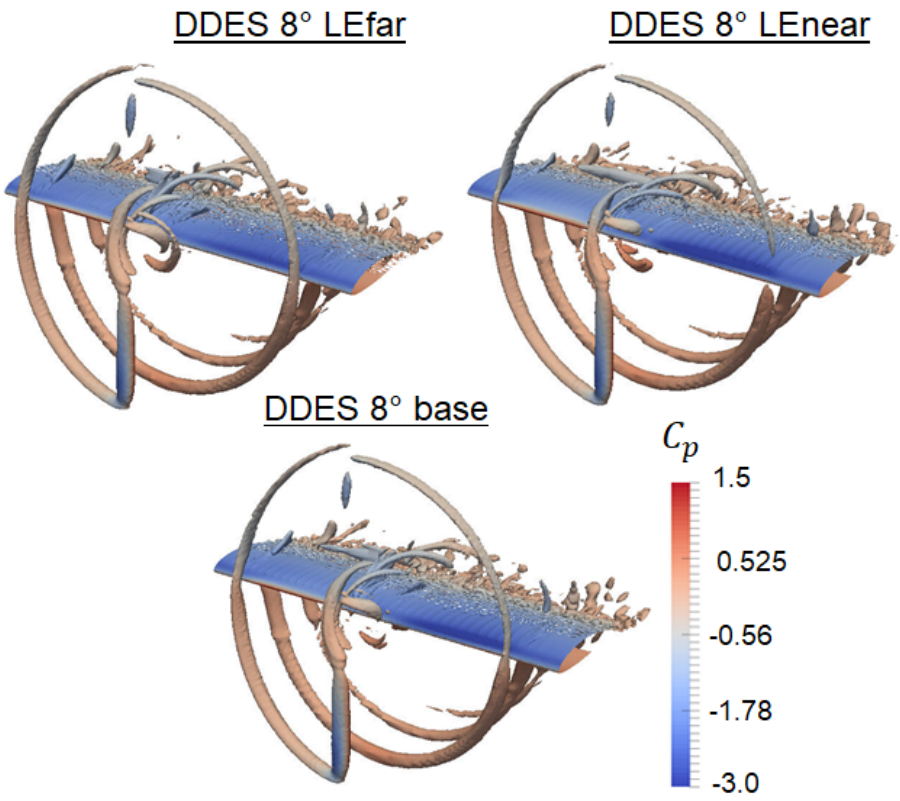

Figure 10: Comparison of instantaneous vortex structures: rotor-wing chordwise separation

compared to baseline. Clearly, the L/D ratio is very sensitive to changes in drag due to the low overall values of drag seen in the infinite wing configuration compared to a finite wing.

Table 1: Aggregate rotor-wing quantities: rotor-wing chordwise separation

Quantity	LEnear	Base	LEfar
Power loading (N/W)	0.0331	0.0329	0.033
L/D ratio	19.697	20.649	22.226

Variation of rotor-wing vertical offset

In this subsection, we consider the second geometric parameter, i.e., the rotor-wing vertical offset. This change is expected to show a significant effect on the rotor as well as wing quantities.

Fig. 18 shows a comparison of the instantaneous vortical structures shed from the rotor and the wing for the vertical-offset cases. Several differences can be observed between the three cases: the vertical-offset dramatically influences the shedding of root vortices, particularly for the rotorDown case where root vortices form a tight spiral. Also, the interaction of the tip vortices with the wing is altered due to the vertical offset with baseline and rotorUp cases showing higher levels of interaction due to shed vorticity from the rotor blowing over the wing. Some differences can also be seen in the pressure contours on the wing, with the rotorUp case showing a deeper blue over the wing while the rotorDown case shows overall higher pressure and consequently a lower lift.

For rotor-wing aerodynamic quantities, Fig. 15 shows the phase-averaged integrated rotor thrust and power for the vertical-offset cases. The rotorDown case shows significantly higher thrust over the cycle compared to the baseline case with the peak thrust being 8.93% higher than baseline. On the other hand, the rotorUp case shows a significant decrease in thrust compared to rotorDown and baseline particularly around $\phi = 90^\circ$ when the blade is parallel to the wing. The rotorUp thrust reaches a minima which is found to be 40.1% lower than the baseline. However, it must be noted that due to the vertical offset the blade does not lie in front of the wing at this phase. In fact, these significant differences in thrust around $\phi = 90^\circ$ are due to the rotor blades lying completely above or below the wing, where the flowfield is strongly influenced by the wing-induced circulation. The cycle-averaged thrust for rotorUp is found to be 6.915

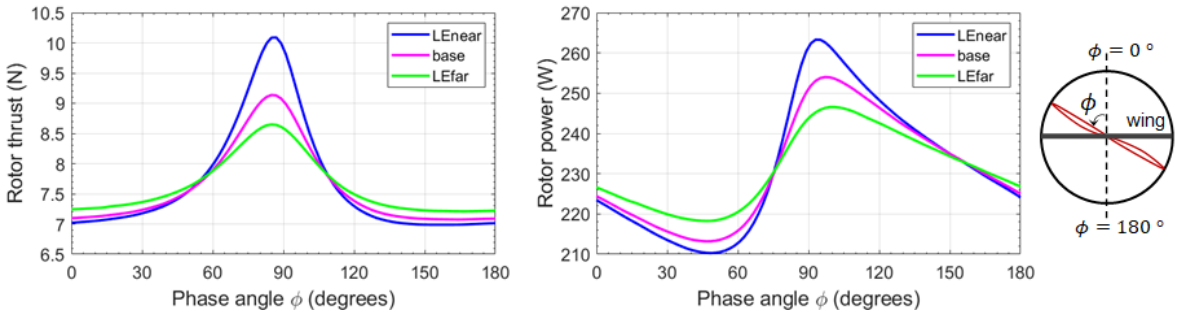

Figure 11: Comparison of phase-averaged rotor thrust and power: rotor-wing chordwise separation

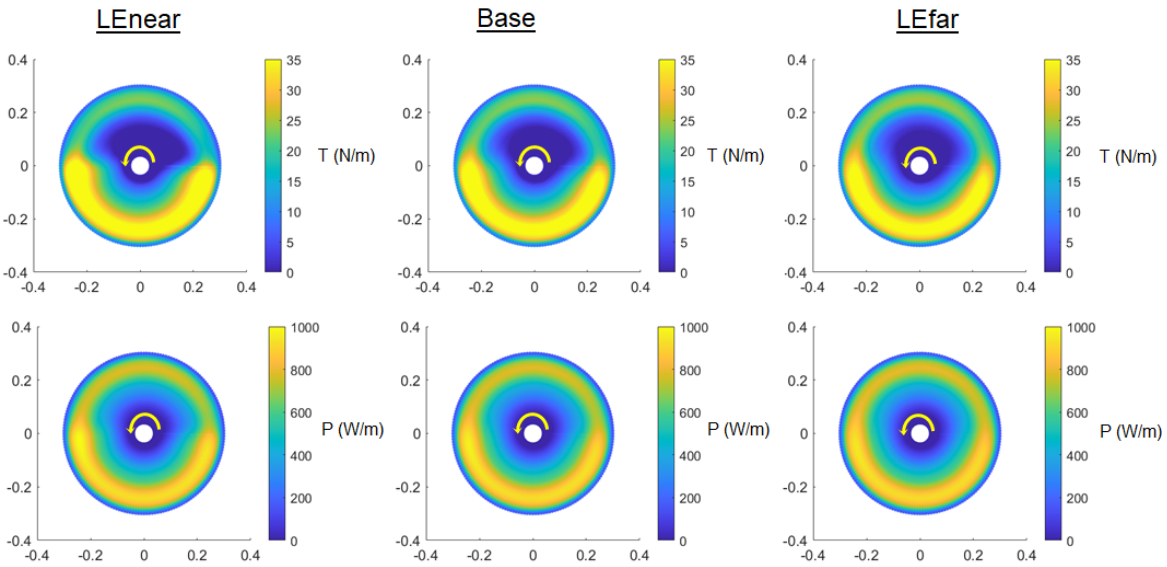

Figure 12: Comparison of thrust and power disk plots: rotor-wing chordwise separation

N which is 9.01% lower than the baseline case with 7.6 N while the rotorDown case results in 8.357 N which is 9.97% higher as compared to the baseline case. The phase-averaged power curves show a similar order with the rotorUp case leading to 225.48 W which is 2.43% lower than the baseline case with 231.1 W while rotorDown results in 237.52 W which is 2.78% higher than baseline. Fig. 16 confirms these observations based on the integrated thrust and power results. The rotorUp case shows lighter colors over a higher area of the rotor disk compared to baseline and the dark yellow contour corresponds to the region below the wing. Conversely, the rotorDown case shows the opposite behavior with the blue region substantially reduced compared to the rotorUp and baseline cases, and the high thrust/power region covering a larger portion of the rotor disk. Fig. 19 shows the time-averaged sectional lift and drag and its spanwise variation for the vertical-offset cases. The rotorUp cases show significantly higher lift over the entire span compared to the baseline and rotorDown cases. Specifically, rotorUp leads to a time-averaged wing lift of 30.54 N which is 4.66% higher than the baseline at 29.18 N, while rotorDown results in a time-averaged lift value of 28.2 N which is 3.36% lower than the baseline. Interestingly, while the rotorDown and baseline cases show largely similar behavior with the rotorDown case showing lower values of lift, rotorUp shows more uniformity in lift over the wing span. All cases show high drag on the downstroke side as expected although rotorUp does show 6.7% lower peak drag compared to the other two cases. On the upstroke side, the rotorUp case shows comparable peak drag to baseline while rotorDown shows 23.53% higher peak drag than the baseline value. For comparison of time-averaged wing drag, rotorUp shows 1.495 N which is 5.8% higher than the baseline case at 1.413 N despite the lower peak drags; this is mainly because of the higher sectional drag seen in the mid-span of the wing, a feature absent in the other two cases. Meanwhile, the

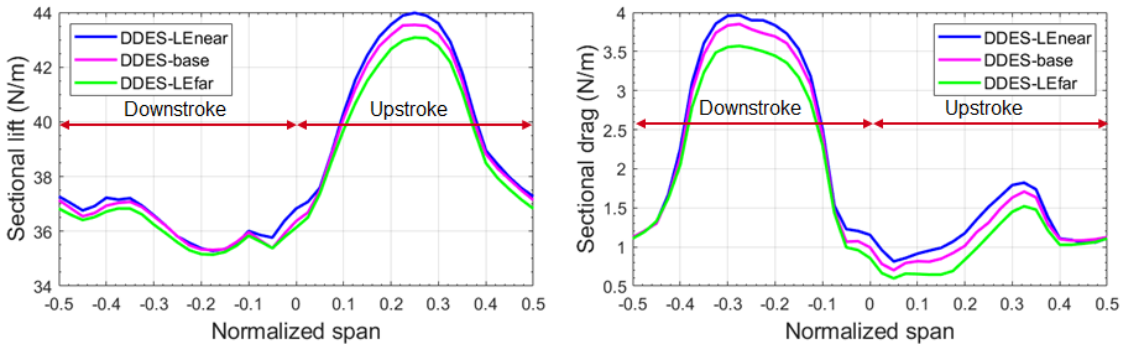

Figure 13: Comparison of spanwise lift and drag: rotor-wing chordwise separation

rotorDown case shows 1.597 N of drag which is 13.02% higher than the baseline drag. Again, we use the aggregate rotor-wing quantities to comprehensively compare the vertical-offset cases as shown in Table 3. Clearly, while the rotorDown case shows a power loading that is 6.99% higher than baseline, its L/D ratio is 14.49% lower than the baseline case. On the other hand, rotorUp provides similar L/D ratio to baseline (within $\sim 1\%$) but shows a 6.69% lower power loading making it less efficient than the baseline configuration. Again, despite the lift increase yielded by the rotorUp case, the overall higher drag hurts the L/D ratio. This conclusion may change in the case of a finite wing where the baseline drag is higher.

Table 2: Aggregate rotor-wing quantities: rotor-wing vertical offset

Quantity	rotorUp	Base	rotorDown
Power loading (N/W)	0.0307	0.0329	0.0352
L/D ratio	20.432	20.649	17.657

Variation of rotor-rotor separation

The final geometric parameter variation considered in this study is the rotor-rotor separation along the wing span. For the infinite rotor-wing case in this work with periodic condition in the spanwise direction, this effectively changes the spanwise extent of the wing section in the simulation. Wing aerodynamic quantities are expected to vary with this change without significantly affecting the rotor quantities.

Fig. 18 shows the instantaneous Q-criterion isosurfaces colored by pressure as done above. The difference in the wing spans can be observed for the rotor-rotor separation cases. The rotorNear case shows the smaller unblown wing section outside the rotor wake while the rotorFar case shows a larger unblown wing section compared to baseline. The lack of deep blue color can be noticed on the unblown wing sections indicating lower lift generation. The shed vorticity from the rotor and its interaction with the wing seems largely unchanged between the three cases.

Comparison of rotor quantities are not presented for this parametric variation as the results are found to be identical to the baseline case for both rotorNear and rotorFar cases. Fig. 19 shows the time-averaged sectional lift and drag for the rotor-rotor separation cases. It must be noted that the x-axis in the sectional lift and drag plots are normalized span and since these cases have different spanwise extents, the peak lift and drag will not occur at the same non-dimensional span location for the three cases. The rotorFar and baseline cases show very simnilar behavior in sectional lift as well as sectional drag. This indicates that the baseline wing span is sufficient to prevent significant effects due to adjacent rotor wakes in the infinite rotor-wing setup. Comparing the overall time-averaged wing lift, rotorFar shows 38.18 N/m which is 0.29% lower than the baseline lift. Values are presented as N/m instead of N to appropriately compare aerodynamic quantities measured over different spans. On the other hand, the rotorNear case shows slightly higher peak lift on the upstroke side compared to the other two cases and shows higher lift on the downstroke side, particularly towards the end of the span indicating the influence of the adjacent rotor wake. Specifically, the overall wing lift is computed to be 39.13 N/m which is 2.19% higher than the baseline. Spanwise drag on the upstroke and downstroke sides shows similar trends in all three cases with the rotorNear case showing marginally lower peaks but covers a larger extent of the span. Specifically, rotorNear shows 1.855 N/m of drag which is within 0.2% of the baseline at 1.854 N/m. On the other hand, rotorFar shows 1.75 N/m of drag, which is 5.61% lower than the baseline. As done earlier, Table 3 shows the aggregate wing and rotor quantities for the rotor-rotor separation study. As expected, the thrust/power ratio are identical across the three cases. Interestingly, both the rotorNear and rotorFar

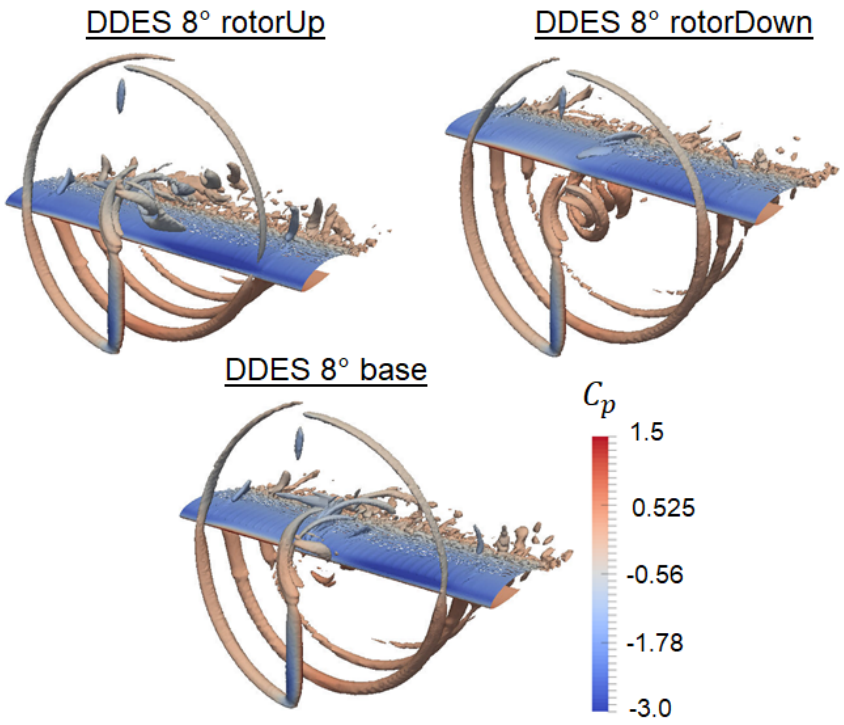

Figure 14: Comparison of instantaneous vortex structures: rotor-wing vertical offset

cases show higher L/D ratios compared to baseline with rotorFar showing the highest L/D ratio despite showing similar lift profiles to baseline. This is due to the lower drag over larger unblown sections of the wing increasing its L/D ratio by 5.66%. The rotorNear case does not show highest L/D ratio (2.16% higher than baseline) despite showing higher sectional lift compared to the other two cases due to the lack of low drag wing sections towards either end of the span.

Table 3: Aggregate rotor-wing quantities: rotor-rotor separation

Quantity	rotorNear	Base	rotorFar
Power loading (N/W)	0.0329	0.0329	0.0329
L/D ratio	21.094	20.649	21.818

CONCLUDING REMARKS

An infinite rotor-wing unit based on the CRC-20 quad-rotor bi-plane was modeled at an angle of attack of 8° using LES and DDES turbulence modeling approaches. This work comprehensively analyzed the rotor-wing configuration by parametrically varying features of the geometry including rotor-wing chordwise separation, rotor-wing vertical offset, as well as rotor-rotor spanwise separation. The rotor was modeled using an ALM approach to balance computational cost while capturing key flow features. The baseline configuration was modeled using LES and two flavors of the DDES - one without and one with the transition model (γ transition model was used). ALM-DDES with transition model was chosen for the parametric study as it showed better agreement in lift with ALM-LES. The baseline rotor-wing case was then compared with isolated wing and rotor cases to quantify the effect of rotor-wing aerodynamic interactions. The rotor-wing case showed 5.46% lower power loading compared to the isolated rotor while the baseline wing showed a 14.42% higher lift and a 4.45% higher L/D ratio of 20.65 compared to the isolated wing at 19.77.

From the parametric variation of the rotor-wing geometry, it was observed that changing the rotor-wing chordwise separation did not significantly affect the rotor power loading but the L/D ratio for the LEfar case was 7.64% higher than baseline while LEnear showed a 4.61% lower L/D ratio. Varying the rotor-wing vertical offset resulted in significant changes to the overall aerodynamics of the rotor-wing unit. The rotorDown case showed a 6.99% higher power loading compared to baseline but a 14.49% lower L/D ratio, while the rotorUp case provides similar L/D ratio to the baseline but is accompanied by a 6.69% lower power loading. Finally, changing the spanwise rotor-rotor separation yielded no significant changes to the rotor aerodynamics but did influ-

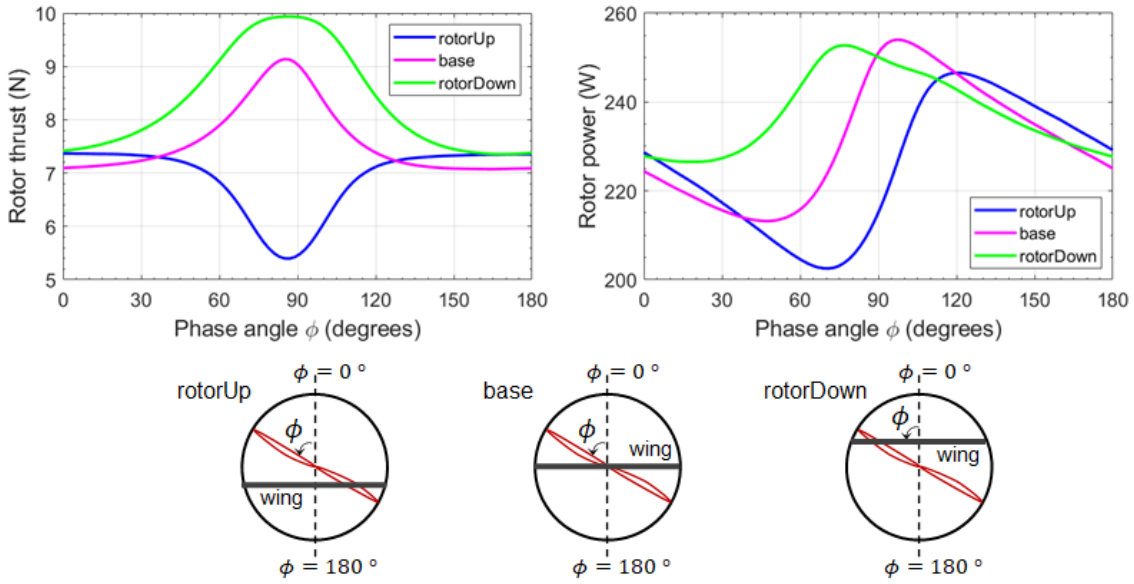

Figure 15: Comparison of phase-averaged rotor thrust and power: rotor-wing vertical offset

ence the wing aerodynamics. The rotorNear case showed higher lift than the other two cases and yielded a 2.16% higher L/D ratio compared to baseline. The rotorFar case showed an even higher L/D ratio of 5.66% despite no increase in sectional lift because of the longer low drag sections at either end of the wing section. From the parametric study, the LEfar (rotor placed further from wing) and rotorFar (higher rotor-rotor separation) showed the highest L/D ratio gains without adverse effects on rotor performance, mainly due to reduction in sectional drag which significantly affects the infinite wing L/D ratio. Future work for this study includes a deeper investigation into the aerodynamics surrounding the geometry variations considered in this study and an extension of this analysis to finite-wing configurations.

REFERENCES

1. R. Singh, J. Sirohi, and V. Hrishikenvan. Common research configuration for collaborative advancement of scalable VTOL UAS technologies. In *75th Annual Forum of the American Helicopter Society*, 2019.

2. P. Aref, M. Ghoreyshi, A. Jirasek, M.J. Satchell, and K. Bergeron. Comp. study of prop.–wing aero. interaction. *Aerospace*, 5:79, 2018.

3. J.S. Fischer and B. Ortun. Simulation & analysis of the aerodynamic interaction between distributed propulsion and wings. In *AHS Technical Meeting on Aeromechanics Design for Transformative Vertical Flight*, 2018.

4. M. Misiorowski, F. Gandhi, and P. A-Inthra. Comp. analysis of rotor-blown-wing for elec. rotorcraft apps. *AIAA J.*, 2020.

5. Ullhas Hebbar, Onkar Sahni, and Farhan Gandhi. Comparison of numerical modeling approaches for flow over a wing with an upstream rotor. In *AIAA SCITECH 2022 Forum*, page 1332, 2022.

6. T. CA Stokkermans, N. van Arnhem, T. Sinnige, and L. LM Veldhuis. Validation and comparison of RANS propeller modeling methods for tip-mounted applications. *AIAA Journal*, 57:566–580, 2019.

7. T. Sinnige, N. van Arnhem, T. CA Stokkermans, G. Eitelberg, and L. LM Veldhuis. Wingtip-mounted propellers: Aerodynamic analysis of interaction effects and comparison with conventional layout. *J. of Aircraft*, 56:295–312, 2019.

8. N. van Arnhem, R. de Vries, R. Vos, and L. LM Veldhuis. Aerodynamic performance of an aircraft equipped with horizontal tail mounted propellers. In *AIAA Aviation 2019 Forum*, 2019.

9. Jens N Sørensen, Robert F Mikkelsen, Dan S Henningson, Stefan Ivanell, Sasan Sarmast, and Søren J Andersen. Simulation of wind turbine wakes using the actuator line technique. *Philosophical Transactions of the Royal Society A: Mathematical, Physical and Engineering Sciences*, 373(2035): 20140071, 2015.

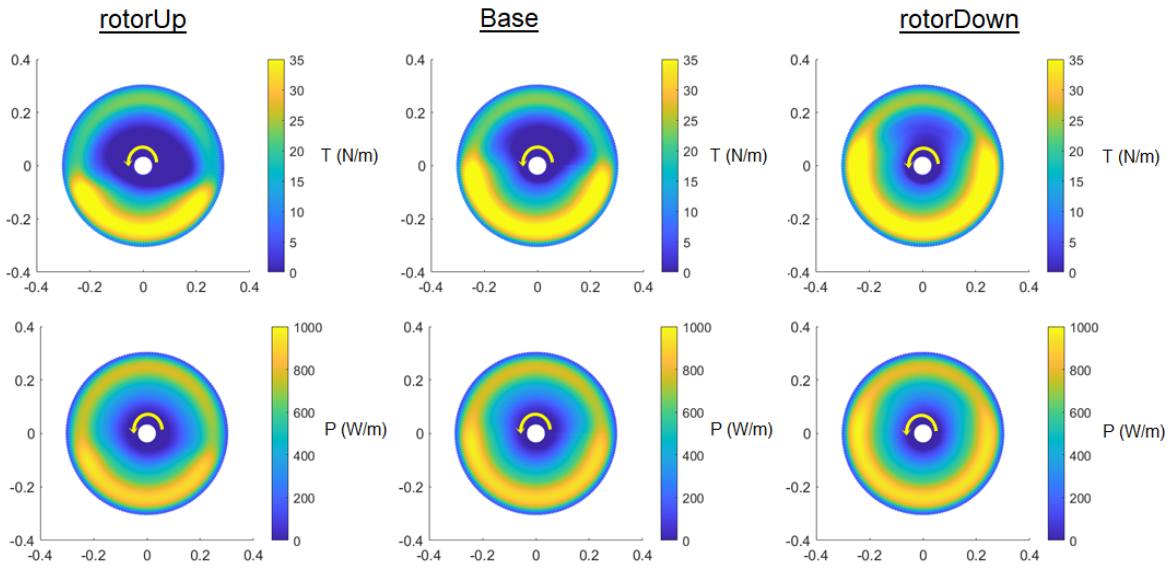

Figure 16: Comparison of thrust and power disk plots: rotor-wing vertical offset

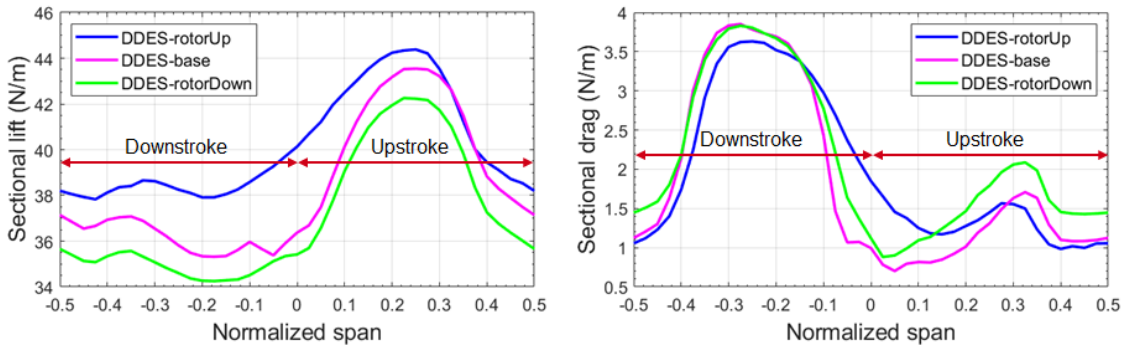

Figure 17: Comparison of spanwise lift and drag: rotor-wing vertical offset

10. Ullhas Hebbar, Jitesh D Rane, Farhan Gandhi, and Onkar Sahni. Analysis of interactional aerodynamics in multi-rotor wind turbines using large eddy simulations. In *AIAA Scitech 2020 Forum*, page 1489, 2020.

11. S. Conley, C. Russell, K. Kallstrom, W. Koning, and E. Romander. Comparing RotCFD predictions of the multirotor test bed with experimental results. In *VFS 76th Annual Forum*, 2020.

12. E. McGlynn, S. Tran, and O. Sahni. LES of flow interactions of seg. synthetic jets on an airfoil. In *2017 AIAA FD Conf.*

13. J. Rane and O. Sahni. LES of surging airfoils at high adv. ratio and Reynolds number. In *2018 AIAA Applied Aero. Conf.*

14. S. Tran and O. Sahni. FE-based LES using a comb. of VMS and dynamic Smag. model. *J. of Turb.*, 18: 391–417, 2017.

15. David Corson, Rajeev Jaiman, and Farzin Shakib. Industrial application of RANS modelling: Capabilities and needs. *International Journal of Computational Fluid Dynamics*, 23(4):337–347, 2009. doi: 10.1080/10618560902776810. URL https://doi.org/10.1080/10618560902776810.

16. Altair HyperWorks CFD AcuSolve. Turbulent flow over a NACA 0012 airfoil. Technical report, . URL https://2021.help.altair.com/2021/hwsolvers/acusolve/topics/acusolve/turbulent_flow_over_a_naca_airfoil.htm. Accessed 18th April 2022.

17. Altair HyperWorks CFD AcuSolve. Laminar to tur-

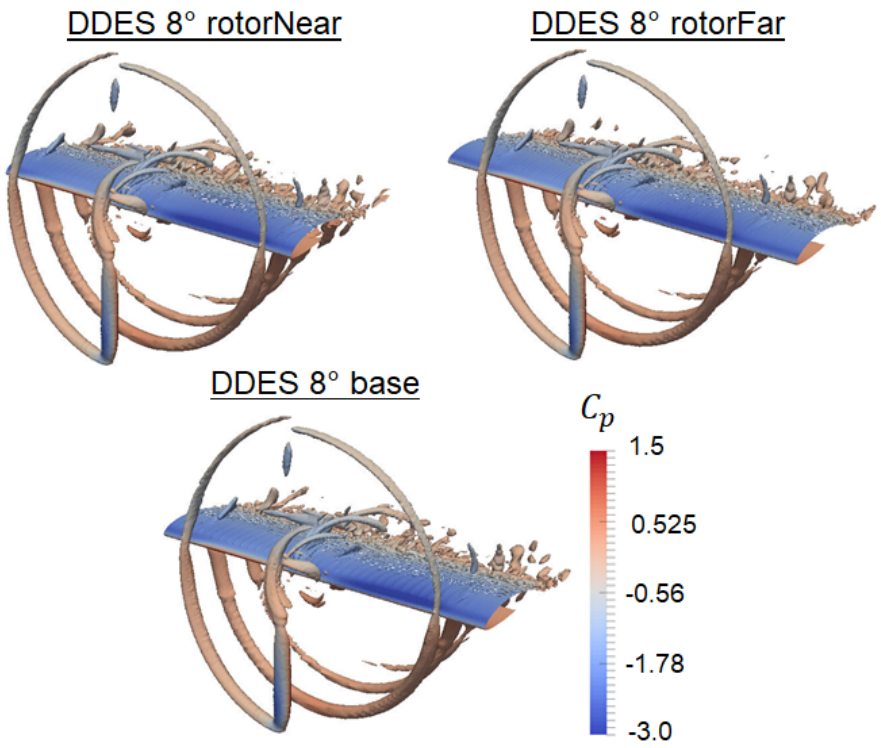

Figure 18: Comparison of instantaneous vortex structures: rotor-rotor separation

bulent transition over an airfoil. Technical report, . URL https://2021.help.altair.com/2021/hwsolvers/acusolve/topics/acusolve/laminar_to_turbulent_transition_over_an_airfoil.htm. Accessed 18th April 2022.

18. Shivaji Medida, David A Corson, and Michael Barton. Implementation and validation of correlation-based transition models in acusolve. In *46th AIAA Fluid Dynamics Conference*, page 3478, 2016.

19. C.R. Russell and M.K. Sekula. Comprehensive analysis modeling of small-scale UAS rotors. In *VFS 76th Annual Forum*, 2020.

20. Kenneth E Jansen, Christian H Whiting, and Gregory M Hulbert. A generalized-α method for integrating the filtered navier–stokes equations with a stabilized finite element method. *Computer Methods in Applied Mechanics and Engineering*, 190(3-4):305–319, 2000.

21. R. Niemiec and F. Gandhi. Development and validation of the Rensselaer multicopter analysis code (RMAC): A physics-based comprehensive modeling tool. In *75th Annual Forum of the American Helicopter Society*, 2019.

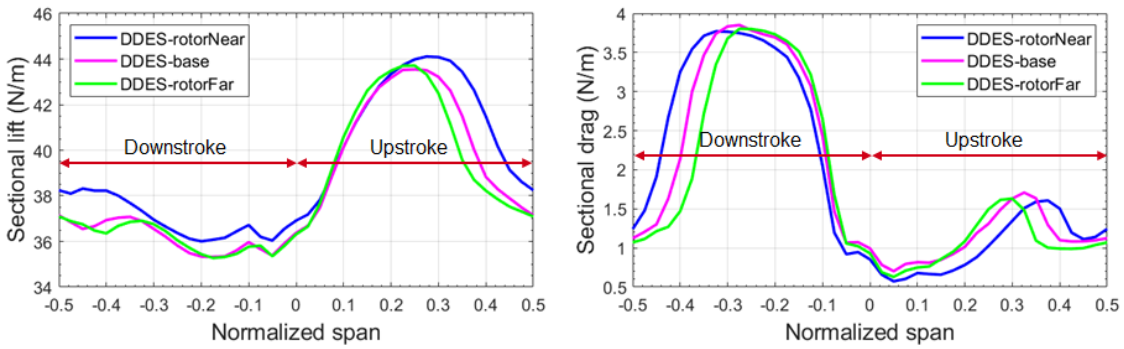

Figure 19: Comparison of spanwise lift and drag: rotor-rotor separation